Research Article

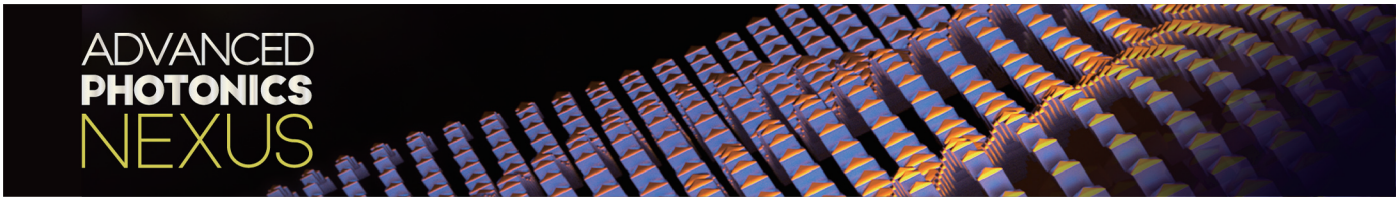

Multimode fiber speckle Stokes polarimeter

Yuxuan Xiong,[a,b] Ting Jiang,[a,b] Hao Wu,[a,b,*] Zheng Gao,[a,b] Shaojun Zhou,[c] Zhao Ge,[a,b] Siqi Yan,[a,b] and Ming Tang[a,b,*]

[a]Huazhong University of Science and Technology, School of Optical and Electronic Information, Wuhan National Laboratory for Optoelectronics, Wuhan, China

[b]Huazhong University of Science and Technology, School of Optical and Electronic Information, Next Generation Internet Access National Engineering Laboratory, Wuhan, China

[c]Huazhong University of Science and Technology University, School of Mechanical Science and Engineering, Wuhan, China

Abstract. The detection of the state of polarization (SOP) of light is essential for many optical applications. However, cost-effective SOP measurement is a challenge due to the complexity of conventional methods and the poor transferability of new methods. We propose a straightforward, low-cost, and portable SOP measurement system based on the multimode fiber speckle. A convolutional neural network is utilized to establish the mapping relationship between speckle and Stokes parameters. The lowest root-mean-square error of the estimated SOP on the Poincaré sphere can be 0.0042. This method is distinguished by its low cost, clear structure, and applicability to different wavelengths with high precision. The proposed method is of great value in polarization-related applications.

Keywords: multimode fiber; state of polarization; polarimeter.

Received Feb. 29, 2024; revised manuscript received May 10, 2024; accepted for publication Jun. 12, 2024; published online Jul. 9, 2024.

[DOI: 10.1117/1.APN.3.4.046010]

1 Introduction

The estimation of the state of polarization (SOP) is critical in various fields, such as optical communications,[1] radar imaging,[2] and solar astronomy.[3] Polarimeters, instruments designed to measure the SOP of light, have received significant attention. Formerly, the focus was primarily on the linearly polarized light and was concentrated on measuring the initial three components of the Stokes vector.[4,5] During this period, information about the circularly polarized state, associated with the fourth component, was not obtainable.[6,7] Subsequently, comprehensive polarimeters capable of measuring the full Stokes vector were investigated. However, conventional SOP measuring methods, such as the rotating quarter-wave plate technique, necessitate the employment of optical elements like polarizers. The inclusion of diverse optical components increases the complexity of the system, and the measurement results are sensitive to environmental noise. Therefore, it is necessary to explore a simple and effective SOP measurement. Apart from traditional methods, metasurfaces, engineered with designed micronanostructures, have been utilized to conduct SOP measurements with enhanced system compactness.[8–10] Nonetheless, they present challenges in design and manufacturing, coupled with limited adjustability and reconfigurability. Furthermore, fibers have been employed to detect SOP, due to their inherent polarization sensitivity.[11] Based on the theory of multicore polarization interference,[12] researchers have utilized three-core photonic crystal fibers for SOP measurement. However, this approach can only detect left- and right-handed polarized lights with varying elliptical polarizations. Moreover, the utilization of photonic crystal fibers results in considerable expense. Therefore, there is an urgent need to develop a compact and cost-effective system for measuring the Stokes parameters of light.

Considering easy implementation and cost reduction, the multimode fiber (MMF) emerges as an economically practical and lightweight alternative.[13] The large core diameter of the MMF enables the excitation of multiple modes with different phase velocities, and these applications are based on the principle of mode coupling. The coupling of the different modes leads to speckle patterns with light and dark features at the output. The speckle patterns contain both amplitude distribution and phase information for all modes.[14–16] Changes in the external environment or input light induce the relative phase between

*Address all correspondence to Hao Wu, wuhaoboom@hust.edu.cn; Ming Tang, tangming@mail.hust.edu.cn

modes and affect the speckle. Thus it is feasible to establish a correlation between the measurement to be conducted and the speckle. The MMF has been employed for the sensors of external factors,[17] such as temperature,[13,18] curvature,[19–21] reflective index,[16] and magnetic field.[22] It also has applications in endoscopy and the transmission of complex images,[14,23,24] and has also proven to be an effective medium for measuring the properties of incident light.[25,26] The above application can be achieved by solving the transmission matrix of an MMF to establish the mapping of inputs and outputs.[27] However, gradual changes in the external environment can impact the transmission matrix, leading to an accumulation of errors during the transmission process.[28] To keep the system stable, researchers have protected MMFs from external interference or developed interference-insensitive MMFs. Others have applied a real-time recalibration of the transmission matrix of the MMF.[29] In addition, researchers employ neural networks to establish mapping relationships between speckles and the parameters to be measured in order to enhance the robustness of measurement systems based on MMF speckle.[25,30] We have verified that the tolerance of MMF to environmental noise can be improved by a convolutional neural network (CNN) in our previous experiments.[31] As a result, measurement of input light SOP can be achieved by monitoring and analyzing the speckle patterns generated by the MMF.

In this paper, we demonstrate an MMF speckle Stokes polarimeter. Multiple MMF speckles were obtained by changing input SOPs. We employed a CNN to efficiently establish a correlation between SOP and speckle intensity distribution. The system does not require optical alignment and laborious microstructure design. The MMF mitigates system complexity and cost and enables applicability for different wavelengths. The CNN excludes environmental impacts, thereby enhancing efficiency and flexibility. For applications related to polarization, the proposed method has significant value.

2 Principle

The distribution of light intensity emitted from the MMF can be explained by Eq. (1), which is a result of different modes of coupling.[32] In Eq. (1), the amplitude and complex phase of the mth mode are represented by a_m and ϕ_m. M denotes the number of modes. Interference occurs on the end facet of an MMF between different modes. If the phase delay between modes is 2π (or a multiple of that), the interference is constructive. If it is π, the interference is destructive. Other possible phase delays produce partially destructive or partially constructive intermediate interferences, ultimately forming a bright and dark scattering pattern at the other end of the MMF.[33] Change in the input SOP will alter the phase difference between the x- and y-polarization quantities, changing the complex phase of modes, thereby affecting the intensity distribution,

$$I(x,y) = |A(x,y)|^2 = \sum_{m=1}^{M}\sum_{n=1}^{M} a_m a_n \exp[j(\phi_m - \phi_n)]. \tag{1}$$

After obtaining speckles related to SOPs from MMF,[26] a CNN is employed to establish a mapping relationship between them. The reason for using a CNN is its wide range of applications in image classification and segmentation.[34,35] Research has demonstrated the effectiveness of CNN in complex nonlinear modeling and classification tasks for detecting intensity within MMF transmission systems.[30,36] Furthermore, this approach eliminates the requirement for additional reference structures and solves the problems associated with minor temperature drift in MMF transmission.[14] Therefore, the subsequent task is to denote the SOPs as CNN labels,

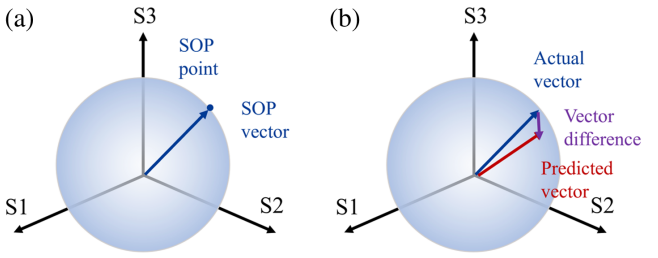

Fig. 1 (a) SOP with known Stokes parameters can be equated to a point on a sphere of radius S_0 with coordinates (S_1, S_2, and S_3), or a vector pointing to the point (S_1, S_2, and S_3) from the origin. (b) Length of vector difference between actual and predicted SOP vectors is utilized to describe the error of the system.

$$S_0^2 = S_1^2 + S_2^2 + S_3^2. \tag{2}$$

Most optical instruments have difficulty in the measurement of high-frequency complex-valued electric and magnetic fields directly.[32] To accurately and comprehensively describe the polarization state of light in measurable quantities, Stokes introduced the Stokes parameters (or Stokes vectors) $[S_0, S_1, S_2, S_3]$.[37] The vector contains four optically measurable quantities and they satisfy the relationship shown in Eq. (2). On the basis of Eq. (2), Henri Poincaré proposed the Poincaré sphere for a clear and graphical representation of SOPs. Each SOP corresponds to a point on the surface of the sphere.[38] An SOP with known Stokes parameters $[S_0, S_1, S_2, S_3]$ can be considered as a point on a sphere of radius S_0 with coordinates (S_1, S_2, S_3), or as a vector that points from the origin $(0,0,0)$ to the point (S_1, S_2, S_3), as depicted in Fig. 1(a). For polarized light, S_0 equals 1.

During the measurement process, there is a natural discrepancy between the predicted and actual vectors, as depicted in Fig. 1(b). The root-mean-square error (RMSE) is often used as a criterion for the estimation accuracy of this discrepancy.[39] Thus it can act as the loss function of the CNN. Though S_0 is fixed, it is still involved in network learning to constrain the other three Stokes parameters. The RMSE of S_0 theoretically converges to 0. So the physical meaning of the entire RMSE is approximated as the length of the difference between the two Stokes vectors, as shown in Fig. 1(b), which is utilized to evaluate the accuracy of measurements.

3 Experimental Setup

The experimental setup is shown in Fig. 2. The wavelength of the laser is 1550 nm. MMF (SI 105/125-22/250, YOFC) has a core diameter of 105 μm and a length of 10 m. In the measurement process, it is necessary to modulate the light of a known fixed SOP to achieve an output of an arbitrary SOP to be measured. Therefore, the Mueller matrix is introduced as a 4×4 order matrix describing the matrix of the change in SOP during transmission and its Stokes parameters are calculated mathematically. Multiplying the Stokes parameter of the incident

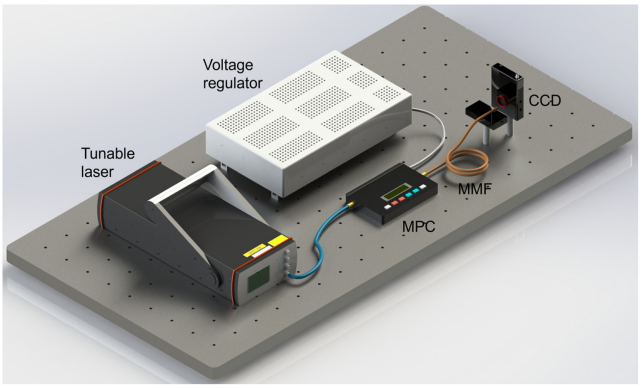

Fig. 2 Scheme of the experimental setup for SOP adjustment and speckle collection.

light and the Mueller matrix of the transmission medium gives the Stokes parameter of the outgoing light after passing through the transmission medium,[4,5] as shown in Eq. (3). The programmable motorized polarization controller (MPC) consisting of two autonomous quarter-wave plates is utilized to achieve arbitrarily polarized outputs, as shown in Fig. 3(a). The plates possess the ability to rotate between 0 and 225 deg, with a precision of 0.225 deg per step. Later in the text, the degree of rotation will be expressed based on the step of rotation. These dual quarter-wave plates, which can be adjusted independently by software, enable one to produce any SOP output to be used as the input of MMF. The CCD (SP620U-1550, Spiricon, image resolution 1200×1600) captures the intensity distribution of the speckle patterns corresponding to different SOPs from MMF, as presented in Fig. 3(b). The 1×4 matrix below each speckle is the corresponding Stokes parameters,

$$S' = MS = \begin{bmatrix} S_{0'} \\ S_{1'} \\ S_{2'} \\ S_{3'} \end{bmatrix} = \begin{bmatrix} m_{00} & m_{01} & m_{02} & m_{03} \\ m_{10} & m_{11} & m_{12} & m_{13} \\ m_{20} & m_{21} & m_{22} & m_{23} \\ m_{30} & m_{31} & m_{32} & m_{33} \end{bmatrix} \begin{bmatrix} S_0 \\ S_1 \\ S_2 \\ S_3 \end{bmatrix}. \quad (3)$$

The image size of the speckle after cropping is 600×600. To minimize loading time, all data have been preprocessed. A 3×3 kernel is employed to perform maximum pooling on the region, resulting in a 200×200 input for the CNN. Through this process, pertinent information is encompassed, and the loading time for the CNN is reduced. The CNN architecture employed is illustrated in Fig. 4, which consists of several residual blocks, convolution, and pooling layers. To better extract detailed information, reduce the number of parameters, and avoid overfitting, the convolutional layers do not change the length or width of the input; it only changes the number of channels, and the dimensionality is reduced mainly through the pooling of the layers. The final fully connected layer generates an estimated value of Stokes parameters. The learning rate, batch size, and epoch are set to 0.001, 128, and 100.

4 Results and Discussion

4.1 Stokes Parametric Measurement

Investigating the capability of the system required an SOP data set covering the full Poincaré sphere. We regulated the SOP through MPC adjustment with a rotational angle of 4.5 deg (20 steps). Two quarter-wave plates rotated from 0 to 225 deg individually and 2600 images were collected as a group, resulting in an SOP distribution traversing the entire Poincaré sphere. It should be noted that although the rotation of the MPC increases linearly, its impact on the Mueller matrix is nonlinear.

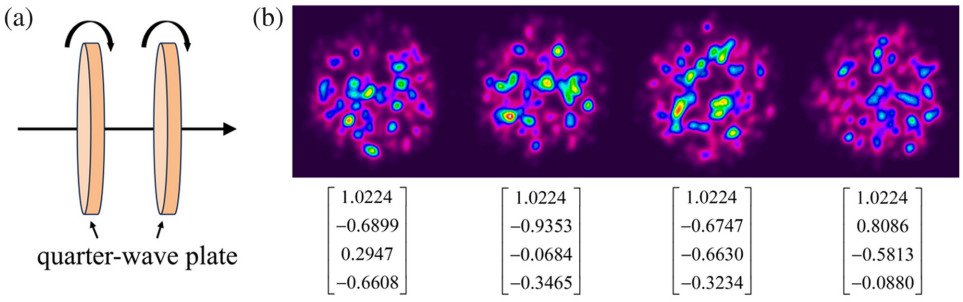

Fig. 3 (a) MPC contains two individually rotatable quarter-wave plates. (b) The speckle patterns with different SOPs are captured by CCD, and the corresponding Stokes parameters are shown under the speckles.

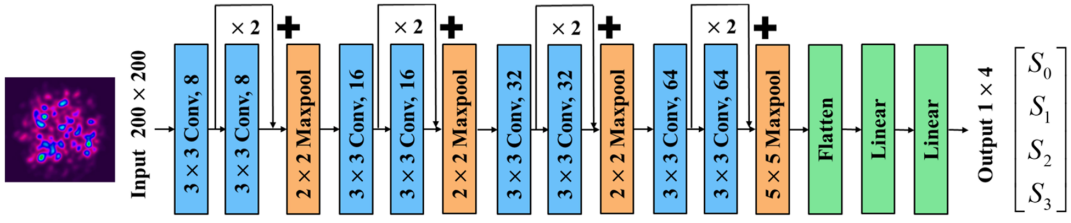

Fig. 4 Structure of CNN mapping SOP to speckle.

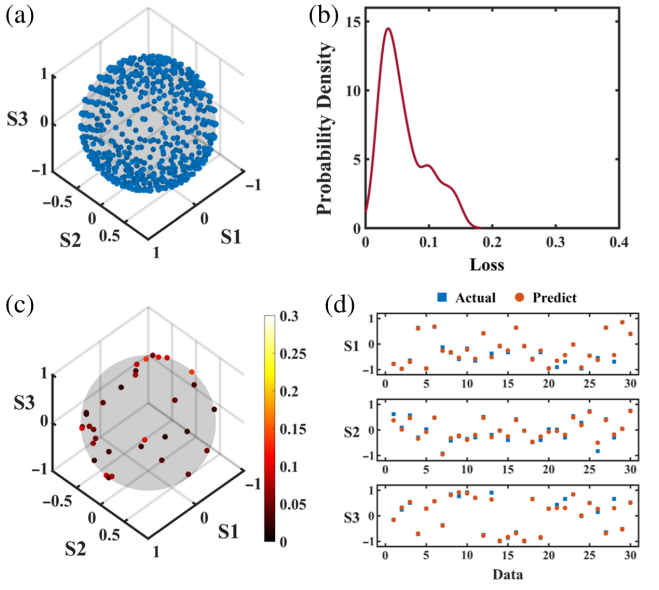

Fig. 5 Data set of SOPs with a rotation step size of 20 and covering the entire Poincaré sphere. (a) Distribution of SOPs on the Poincaré sphere. (b) Distribution of RMSEs related to SOPs. (c) The RMSEs corresponding to points in the test set. (d) Comparison of actual and predicted Stokes parameters.

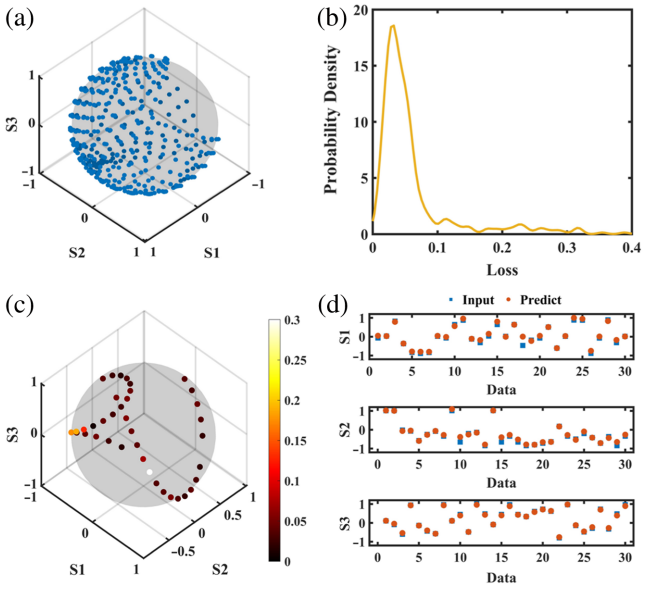

Fig. 6 Data set of SOPs with a rotation step size of 20 covering part of the Poincaré sphere. (a) Distribution of SOPs on the Poincaré sphere. (b) Distribution of RMSEs related to SOPs. (c) The RMSEs corresponding to points in the test set. (d) Comparison of actual and predicted Stokes parameters.

Therefore, some SOPs in the data set were sparse, while others were dense. The data were subjected to a filtering process with the objective of achieving a more uniform distribution across the sphere, which is presented in Fig. 5(a). To eliminate environmental impact, 16 groups of SOPs that covered the entire Poincaré sphere were collected. The data set was divided into a training set, validation set, and test set at an 8:1:1 ratio. In order to evaluate the ability of CNN to predict unknown SOPs, there is no overlap between SOPs in the sets mentioned above. Following the training process, the network generated an RMSE value of 0.0602, which represents the magnitude of the Stokes vector difference between the predicted and actual SOP vectors. For clarity, a distribution function of the loss in the test data set is presented in Fig. 5(b), whereas the RMSE of each point is shown in three-dimensional form in Fig. 5(c). RMSEs of the four Stokes parameters in the test data set are 0.0189, 0.0783, 0.1076, and 0.0694. It should be noted that although S_0 is a fixed value, it is still included in the label and used in the training process due to the relationship between the Stokes parameters, as shown in Eq. (2). The inclusion of S_0 as a physical constraint in the learning process reduces the RMSE and facilitates network convergence. For clear visualization of the precision of the Stokes parameters prediction, we randomly selected 30 SOPs from the test set and illustrated a comparative graph of their predicted and actual Stokes parameters values (S_1, S_2, and S_3) in Fig. 5(d). The outcome demonstrates the capability of the system to measure the four Stokes parameters.

To investigate the influence of polarization range on prediction accuracy, we extracted a partial data set from the global data set, consisting of 20×20 SOPs. (Two quarter-wave plates rotated from 0 to 90 deg, individually.) The RMSE of the partial data set is 0.0658, which is similar to the global data set's RMSE of 0.0602. Both RMSEs are smaller than the vector differences between adjacent SOPs (0.2015). The slight difference of RMSEs between full and partial data sets is caused by the edge SOPs of the partial sphere data set. Figure 6(a) shows the partial SOP distribution. The distribution of partial test data set RMSE is shown in Fig. 6(b). It demonstrates that the measurement accuracy of the system is not related to the range of the SOP. Figures 6(c) and 6(d) depict the RMSE distribution on the Poincaré sphere and predictions corresponding to each Stokes parameter (S_1, S_2, and S_3), respectively.

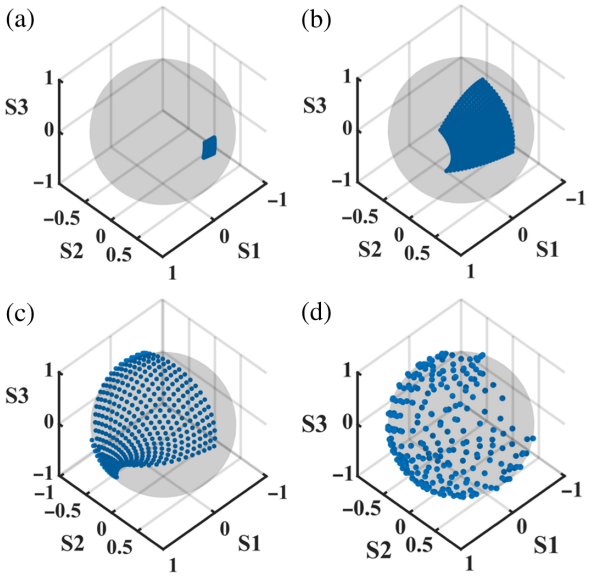

Fig. 7 Distribution of SOP data sets on the Poincaré sphere corresponding to different MPC rotation steps: (a) 1 step, (b) 5 steps, (c) 10 steps, and (d) 20 steps.

4.2 High-Precision Measurement

To improve the estimation accuracy, we reduced the MPC rotation interval to generate denser-distribution data sets of SOPs. The MPC rotation increments are set at 1, 5, 10, and 20 (0.225, 1.125, 2.250, and 4.500 deg). We have demonstrated the accuracy similarity with a step size smaller than 20. Therefore, for each interval, 10 sets of 20×20 SOP speckles were collected (Two quarter-wave plates rotate from 0 deg to 20 times of interval individually as a set). Figure 7 illustrates the distribution of SOPs on the Poincaré sphere with different rotation steps. The density and homogeneity of the SOPs increase as the interval reduces with the same number of SOPs. Additionally, the speckle changes between adjacent SOPs are not distinguishable to human eyes.

Table 1 shows the outcomes for each network. By reducing the MPC rotational angle, the interval between adjacent SOP vectors is diminished, resulting in a more uniform and dense SOP distribution, thus enhancing the measurement precision. The RMSEs are smaller than the corresponding vector difference. Figure 8 depicts the RMSE distribution functions of test data sets, whereas Fig. 9 presents the loss distribution in 3D structure for test data sets with diverse MPC rotation steps. The concentration of the loss distribution increases, and the mean value decreases as the MPC rotation angle decreases, indicating accuracy improvement through training data optimization. Furthermore, as the data set distribution becomes denser and the distribution of neighboring SOPs becomes more linear, the likelihood of sudden large RMSEs decreases, increasing the reliability of measurement. Figure 10 compares the Stokes parameters of 30 selected SOPs in the test data sets, further illustrating that using data with smaller vector difference intervals increases accuracy. The results obtained in experiments were considerably lower than the stated accuracy. It should be noted

Table 1 RMSEs of test data sets with different MPC rotational steps.

MPC Rotational Steps	1	5	10	20
MPC rotation angle interval (deg)	0.225	1.125	2.250	4.500
Vector difference	0.0115	0.0573	0.1091	0.2015
RMSE	0.0042	0.0082	0.0133	0.0658
Precision of S_0	0.0021	0.0032	0.0091	0.0189
Precision of S_1	0.0043	0.0091	0.0144	0.0783
Precision of S_2	0.0050	0.0086	0.0142	0.1076
Precision of S_3	0.0028	0.0063	0.0068	0.0694

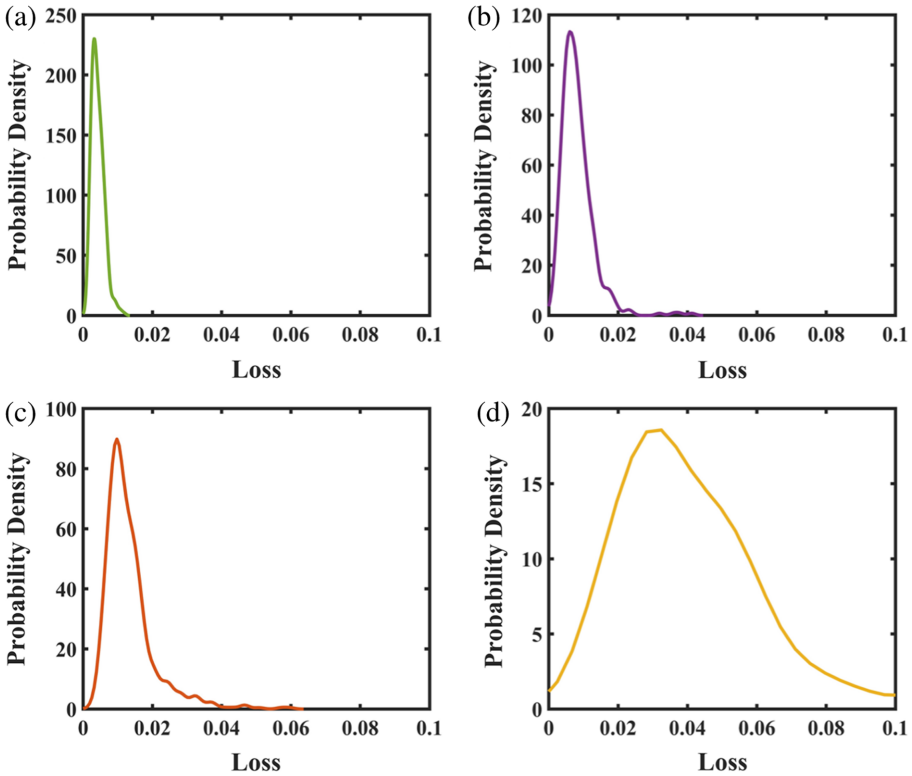

Fig. 8 RMSE distribution of SOPs in test sets with different MPC rotation steps: (a) 1 step, (b) 5 steps, (c) 10 steps, and (d) 20 steps.

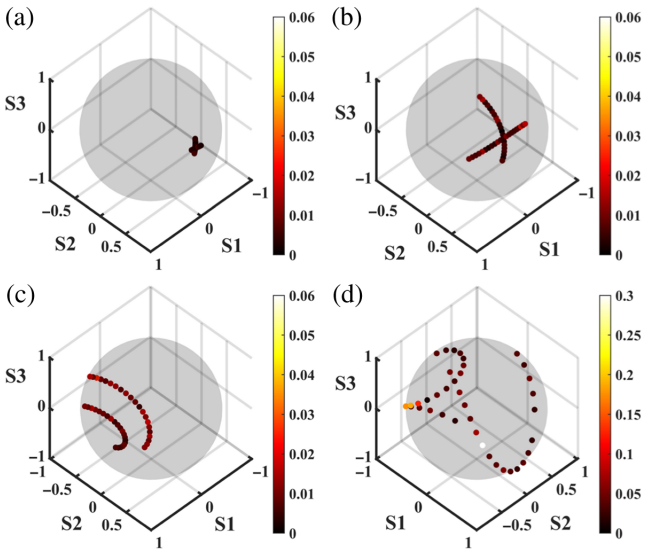

Fig. 9 Loss of SOPs in test sets on the Poincaré sphere corresponding to different MPC rotation steps. SOPs are randomly selected and do not overlap with the training or validation sets. (a) 1 step, (b) 5 steps, (c) 10 steps, and (d) 20 steps.

that with an MPC rotation step size of 1 (0.225 deg), the variations in vector values among different SOPs are minor, and the RMSE is 0.0042. The RMSEs for the four Stokes parameters are 0.0021, 0.0043, 0.0050, and 0.0028, correspondingly. The system measures the four Stokes parameters with similar accuracy and is well-balanced in its sensitivity to each value. This limitation in accuracy is due to the minimum rotation angle of the quarter-wave plate in the MPC. It reveals that the system is capable of achieving highly precise SOP measurements.

4.3 Applicability with Different Wavelengths

Wavelength influences the intensity distribution of speckles.[25] As depicted in Fig. 11(a), the speckles have different intensity distributions with the same SOP at different wavelengths. Therefore, it is imperative to assess the system for its applicability to different wavelengths. Since the measurement principle of the system is similar at different wavelengths and the resolution is mainly related to SOP distribution density, a 10 nm spectral band is used to verify wavelength applicability, and the MPC rotation increment was set at 80 (18 deg). The laser emits light at a single wavelength, ranging from 1545 to 1555 nm in increments of 0.5 nm. And 10 × 10 SOP speckles were collected as a set, as shown in Fig. 11(b). (Two quarter-wave plates rotate from

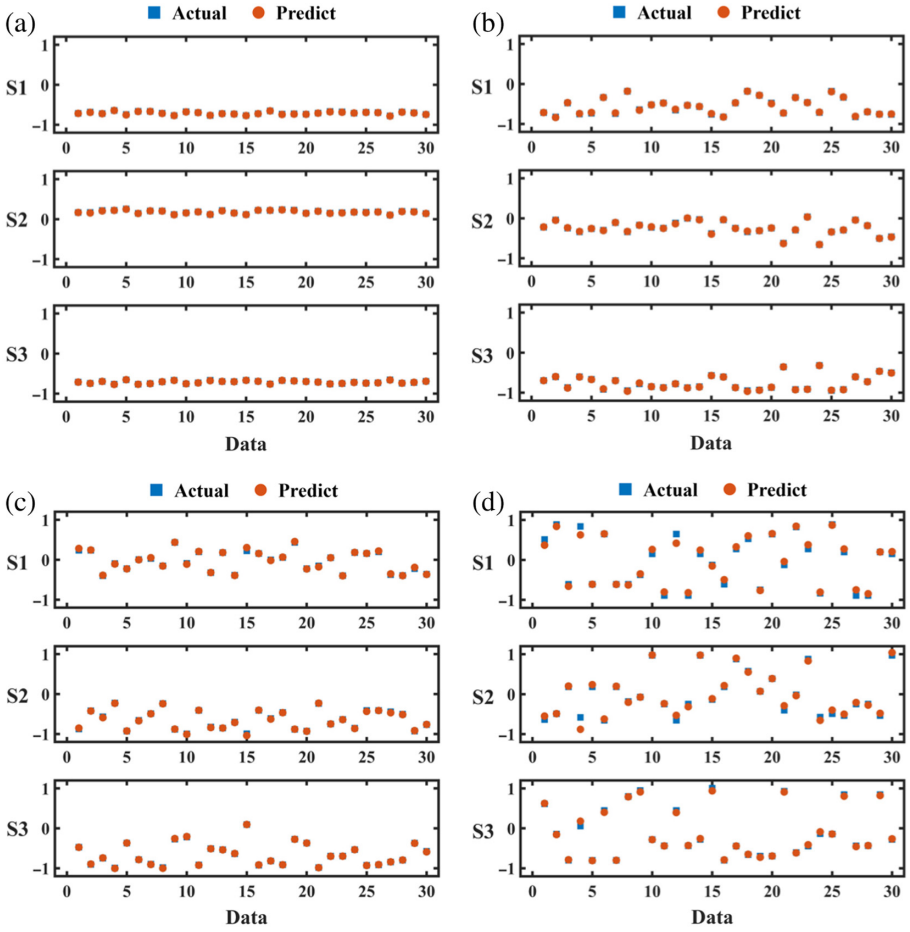

Fig. 10 Comparison of actual and predicted Stokes parameters in test data sets with different MPC rotation steps. (a) 1 step, (b) 5 steps, (c) 10 steps, and (d) 20 steps.

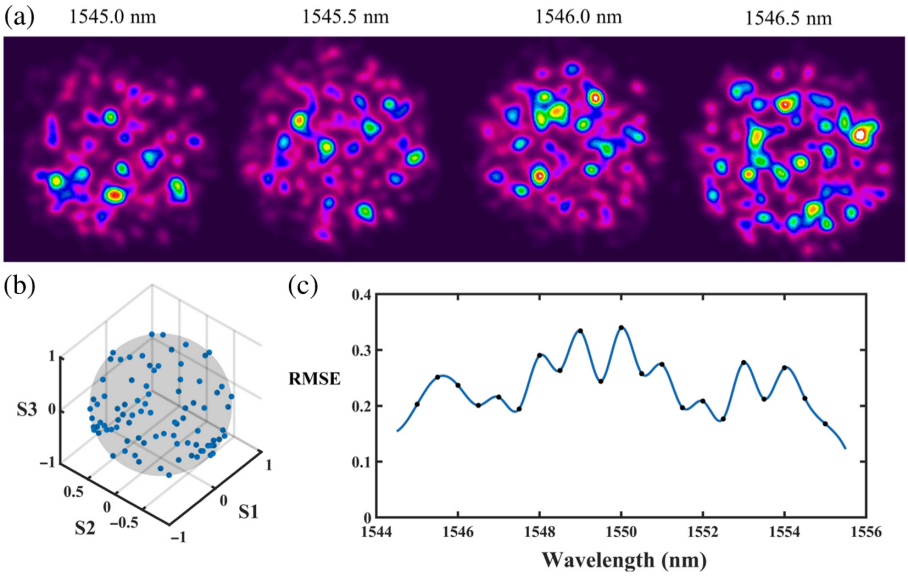

Fig. 11 Test data sets include SOPs with a rotation step size of 80, covering the entire Poincaré sphere. The wavelength interval is 0.5 nm with a bandwidth of 10 nm. (a) The speckles with the same SOP of [1.022465, −0.6899, −0.2947, and 0.6608] at different wavelengths. (b) The distribution of SOPs with different wavelengths. (c) RMSEs of SOPs in the test data sets corresponding to different wavelengths.

0 to 180 deg individually as a set). We collected five sets of SOP speckles, covering the entire Poincaré sphere for each wavelength. The RMSEs for different wavelengths are depicted in Fig. 11(c). The minimum RMSE is 0.1678 at 1555 nm, while the maximum is 0.3400 at 1550 nm. Given that the SOPs in the data set are sparse, these RMSEs are smaller than the interval between adjacent SOPs (0.7415). The results indicate that the largest RMSE occurs at 1550 nm, which is the same wavelength used in the previous experiment. Therefore, using other wavelengths in the system can achieve similar SOP measurement accuracy with similar SOP distribution density, making it applicable to different wavelengths with interest.

5 Conclusion

In this paper, we proposed and demonstrated an MMF speckle Stokes polarimeter. The MMF is employed to generate specific speckle patterns with specified SOPs, while a CNN is utilized to establish a mapping relationship between them. We demonstrate the polarized optical Stokes parametric measurement capability of the system. The system can achieve a minimum RMSE of 0.0042. The RMSEs for the Stokes parameters in this case are 0.0021, 0.0043, 0.0050, and 0.0028, respectively. The system currently performs highly precise single-point polarized optical Stokes parameter measurements at different wavelengths. It enables a low-cost and straightforward Stokes polarimeter that provides great value for polarization-related applications. Also, it has the potential to be used for full Stokes parameter and polarization measurements of complex optical fields in the future.

Disclosures

The authors have no relevant financial interests in the paper and no other potential conflicts of interest to disclose.

Code and Data Availability

The data that support the findings of this study are available from the corresponding author upon reasonable request.

Acknowledgments

This work was supported by the National Key Research and Development Program of China (Grant No. 2021YFB2800902), the National Natural Science Foundation of China (Grant No. 62225110), the Key Research and Development Program of Hubei Province (No. 2022BAA001), and the Innovation Fund of WNLO.

References

1. Z. Yu et al., "Experimental demonstration of polarization-dependent loss monitoring and compensation in stokes space for coherent optical PDM-OFDM," *J. Lightwave Technol.* **32**, 4528–4533 (2014).
2. R. Raney, "Dual-polarized SAR and Stokes parameters," *IEEE Geosci. Remote Sens. Lett.* **3**, 317–319 (2006).
3. J. B. Breckinridge and B. R. Oppenheimer, "Polarization effects in reflecting coronagraphs for white-light applications in astronomy," *Astrophys. J.* **600**, 1091–1098 (2004).
4. D. H. Goldstein, *Polarized Light*, CRC Press (2017).
5. R. M. A. Azzam, "Stokes-vector and Mueller-matrix polarimetry [Invited]," *J. Opt. Soc. Amer. A* **33**, 1396 (2016).
6. V. Gruev, R. Perkins, and T. York, "CCD polarization imaging sensor with aluminum nanowire optical filters," *Opt. Express* **18**, 19087 (2010).
7. A. Andreou and Z. Kalayjian, "Polarization imaging: principles and integrated polarimeters," *IEEE Sens. J.* **2**, 566–576 (2002).
8. D. Wen et al., "Metasurface for characterization of the polarization state of light," *Opt. Express* **23**, 10272 (2015).
9. F. Ding, Y. Chen, and S. Bozhevolnyi, "Metasurface-based polarimeters," *Appl. Sci.* **8**, 594 (2018).

10. J. Qu et al., "Full-Stokes parameters detection enabled by a non-interleaved fiber-compatible metasurface," *Opt. Express* **31**, 20836 (2023).
11. F. Alhassen et al., "All-fiber acousto-optic polarization monitor," *Opt. Lett.* **32**, 841 (2007).
12. Y. Zhao et al., "Three-core photonic crystal fiber for the in-line measurement of full-polarization states by multi-core polarization interference theory," *Opt. Lett.* **48**, 3985 (2023).
13. J. D. Arango et al., "Deep learning classification and regression models for temperature values on a simulated fibre specklegram sensor," *J. Phys. Conf. Ser.* **2139**, 012001 (2021).
14. C. Zhu et al., "Image reconstruction through a multimode fiber with a simple neural network architecture," *Sci. Rep.* **11**, 896 (2021).
15. D. L. Smith et al., "Machine learning for sensing with a multimode exposed core fiber specklegram sensor," *Opt. Express* **30**, 10443 (2022).
16. L. Cai, M. Wang, and Y. Zhao, "Investigation on refractive index sensing characteristics based on multimode fiber specklegram," *Meas. Sci. Technol.* **34**, 015125 (2023).
17. E. Fujiwara et al., "Development of a tactile sensor based on optical fiber specklegram analysis and sensor data fusion technique," *Sens. Actuators A* **263**, 677–686 (2017).
18. R. Hamid and M. I. Cheema, "Use of machine learning in a speckle-based optical fiber sensor for temperature detection," *Proc. SPIE* **12019**, 120190J (2022).
19. H. Gao et al., "Bending recognition based on learning enhanced fiber specklegram sensor," *Meas. Sci. Technol.* **34**, 115125 (2023).
20. G. Li et al., "Deep learning based optical curvature sensor through specklegram detection of multimode fiber," *Opt. Laser Technol.* **149**, 107873 (2022).
21. Y. Liu et al., "Bending recognition based on the analysis of fiber specklegrams using deep learning," *Opt. Laser Technol.* **131**, 106424 (2020).
22. R.-Z. Zhu et al., "Magnetic field sensing based on multimode fiber specklegrams," *J. Lightwave Technol.* **39**(11), 3614–3619 (2021).
23. G. Wu et al., "High-definition image transmission through dynamically perturbed multimode fiber by a self-attention based neural network," *Opt. Lett.* **48**, 2764–2767 (2023).
24. A. Newaz et al., "Machine-learning-enabled multimode fiber specklegram sensors: a review," *IEEE Sens. J.* **23**(18), 20937–20950 (2023).
25. F. Feng et al., "Ai-assisted spectrometer based on multi-mode optical fiber speckle patterns," *Opt. Commun.* **522**, 128675 (2022).
26. O. C. Inalegwu, R. E. G. Ii, and J. Huang, "A machine learning specklegram wavemeter (MaSWave) based on a short section of multimode fiber as the dispersive element," *Sensors* **23**, 4574 (2023).
27. G. Huang et al., "Retrieving the optical transmission matrix of a multimode fiber using the extended Kalman filter," *Opt. Express* **28**, 9487–9500 (2020).
28. S. Angelucci et al., "Structured light enhanced machine learning for fiber bend sensing," *Opt. Express* **32**, 7882–7895 (2024).
29. G. Wu et al., "Optical scanning endoscope via a single multimode optical fiber," *Opto-Electron. Sci.* **3**(3), 230041–1–230041–32 (2024).
30. U. Kürüm et al., "Deep learning enabled real time speckle recognition and hyperspectral imaging using a multimode fiber array," *Opt. Express* **27**, 20965–20979 (2019).
31. Y. Xiong et al., "MMF-based polarization state measurement system with temperature resistance," in *Opto-Electron. and Commun. Conf. (OECC)*, pp. 1–3 (2023).
32. P. Yang, J. Ding, and G. W. Kattawar, "Maxwell's equations for single-scattering partiles," in *Light, Plasmonics and Partiles*, M. P. Mengüç and M. Francoeur, eds., pp. 21–42, Elsevier (2023).
33. A. R. Cuevas et al., "Machine learning for turning optical fiber specklegram sensor into a spatially-resolved sensing system. Proof of concept," *J. Lightwave Technol.* **36**, 3733–3738 (2018).
34. A. Khan et al., "A survey of the recent architectures of deep convolutional neural networks," *Artif. Intell. Rev.* **53**, 5455–5516 (2020).
35. F. Sultana, A. Sufian, and P. Dutta, "Evolution of image segmentation using deep convolutional neural network: a survey," *Knowl.-Based Syst.* **201–202**, 106062 (2020).
36. M. Wei et al., "Neural network based perturbation-location fiber specklegram sensing system towards applications with limited number of training samples," *J. Lightwave Technol.* **39**, 6315–6326 (2021).
37. H. G. Berry, G. Gabrielse, and A. E. Livingston, "Measurement of the Stokes parameters of light," *Appl. Opt.* **16**, 3200 (1977).
38. J. A. Jones et al., "The Poincaré-sphere approach to polarization: formalism and new labs with Poincaré beams," *Amer. J. Phys.* **84**, 822–835 (2016).
39. H. Hu, T. Liu, and X. Li, *Measurement and Imaging Processing of Polarization Information*, Science Press (2022).

Yuxuan Xiong received her BS degree from Huazhong University of Science and Technology (HUST), Wuhan, China, in 2021. She is currently working toward her PhD at the School of Optical and Electronic Information, HUST, Wuhan, China. Her current research interests include multimode fiber, fiber sensors, and optoelectronic systems.

Ting Jiang received her BEng degree in telecommunications engineering from Beijing University of Posts and Telecommunications (BUPT), Beijing, China, in 2020. Since 2020, she has been working toward her PhD at the School of Optical and Electronic Information, HUST, Wuhan, China. Her research interests include optical performance monitoring, machine learning, and digital signal processing.

Hao Wu received his BS, MS, and PhD degrees from HUST, Wuhan, China, in 2013, 2016, and 2019, respectively. His postdoctoral research at HUST was focused on the machine learning algorithms for distributed optical fiber sensing. Since 2024, he has been a research associate at HUST. His current research interests are the integration of artificial intelligence and optical fiber.

Zheng Gao received his BEng degree from the School of Optical and Electronic Information, HUST, Wuhan, China. Since 2020, he has been working toward his PhD at the School of Optical and Electronic Information, HUST, Wuhan, China. His current research interests include multimode fiber and fiber optics sensing.

Shaojun Zhou received his BS degree from Hubei University of Technology, Wuhan, China, in 2021 and his MD degree from HUST, Wuhan, China, in 2024.

Zhao Ge received his BS degree from Jianghan University, Wuhan, China, in 2019 and his MD degree from HUST, Wuhan, China, in 2022. He is currently working toward a PhD at the School of Optical and Electronic Information, HUST, Wuhan, China.

Siqi Yan received his BS and PhD degrees in optics engineering from HUST in 2013 and 2018, respectively. From 2019 to 2021, he worked as a postdoctoral researcher in the Silicon Photonics for Optical Communications Center at the Technical University of Denmark. In November 2021, he joined the HUST as an associate professor. His primary research interests are high-performance silicon/graphene integrated optoelectronics chips and their applications in optical communication systems.

Ming Tang received his BEng degree from HUST in 2001 and his PhD from Nanyang Technological University, Singapore, in 2005. His postdoctoral research at the Network Technology Research Centre was focused on the optical fiber amplifier. From 2009, he was a research scientist in the Tera-Photonics Group, RIKEN, Japan. Since 2011, he has been a professor at HUST. His current research interests include optical fiber-based linear and nonlinear effects for communication and sensing applications.